






Cite this: *RSC Adv.*, 2022, 12, 13820

Received 24th March 2022
Accepted 3rd May 2022

DOI: 10.1039/d2ra01913b

rsc.li/rsc-advances

Electron transport layer assisted by nickel chloride hexahydrate for open-circuit voltage improvement in MAPbI₃ perovskite solar cells†

Pei Dong, Shuai Yuan,  Dongping Zhu,  Yaxin Du, Cheng Mu * and Xi-Cheng Ai *

SnO₂ is a promising electron transport layer (ETL) material with important applications in planar perovskite solar cells (PSCs). However, electron–hole recombination and charge extraction between SnO₂ and the perovskite layer necessitates further exploration. Nickel chloride hexahydrate (NiCl₂·6H₂O) was introduced into the SnO₂ ETL, which significantly increased the power conversion efficiency (PCE) from 15.49 to 17.36% and the open-circuit voltage (*V*_{OC}) from 1.078 to 1.104 V. The improved PCE and *V*_{OC} were attributed to the reduced defect states and increased energy level of the conduction band minimum. This work provides new insights into optimizing the *V*_{OC} and PCE of PSCs.

Introduction

In recent years, the perovskite solar cell (PSC) has been developed as a promising type of solar cell with outstanding advantages such as high photoelectric conversion efficiency, low cost, and simple fabrication.^{1–3} At present, PSCs have achieved a high power conversion efficiency (PCE) of 25.5%.^{4–12} The main technical approach used to improve the PCE of PSCs is through component engineering of the perovskite layer, hole transport layer (HTL), and electron transport layer (ETL).^{13–18} The other method is to optimize the interface performance by adjusting the structure or adding a buffer layer between the interlayers of PSCs.^{19–28}

The quality of the ETL plays an important role in perovskite device performance. TiO₂, one of the most widely used ETL materials, has deep electron trap states, which easily leads to strong electron–hole recombination. ZnO has also been used as an ETL in PSCs due to its low-temperature film preparation and higher charge mobility. However, the PSC readily decomposes owing to the polyhydroxy groups on the surface of the ZnO. The SnO₂ ETL material is widely used in PSCs for high charge mobility and high perovskite compatibility.²⁹ However, the oxygen vacancy in SnO₂ greatly reduces the hole blocking effect, resulting in significant carrier recombination.³⁰ Therefore, the SnO₂ ETL requires modification to reduce ETL defects and improve the performance of PSCs. For example, Liu *et al.* incorporated EDTA into the SnO₂ ETL to enhance the device

performance,³¹ whereas Yang *et al.* doped Ga³⁺ ions into SnO₂ to passivate the defect state in the ETL.³²

Herein, we report a simple and effective method to passivate SnO₂ defects by introducing nickel chloride hexahydrate (NiCl₂·6H₂O) into a SnO₂ precursor solution. NiCl₂·6H₂O not only reduced the trap density, but also increased the energy level of the conduction band minimum of SnO₂ and caused the energy level to better match that of the perovskite. Consequently, a champion PCE of 17.36% with a *V*_{OC} of 1.104 V was achieved, remarkably higher than the relevant reference devices which provided a PCE of 15.49% and *V*_{OC} of 1.078 V.

Experimental section

Materials

All the materials and solvents were used as received without further purification. Fluorine-doped tin oxide (FTO) glasses (1.5 cm × 1.5 cm) were purchased from OPVtech (China). The SnO₂ solution (tin(IV) oxide, 15 wt% hydrocolloid dispersion) was purchased from Alfa Aesar. Lead iodide (PbI₂), methylammonium iodide (MAI), and 2,2',7,7'-tetrakis (*N,N*-di-*p*-methoxyphenylamine)-9,9'-spirobifluorene (spiro-OMeTAD) were obtained from Xi'an Polymer Light Technology. *N,N*-dimethylformamide (DMF), dimethyl sulfoxide (DMSO), chlorobenzene (CB), and 4-*tert*-butylpyridine were acquired from J&K. Lithium bis(trifluoromethylsulfonyl) imide (Li-TFSI) and cobalt(III) FK209 were obtained from Sigma-Aldrich. Nickel dichloride hexahydrate (NiCl₂·6H₂O) and ammonium (NH₃·H₂O) were purchased from Aladdin.

Device fabrication

The FTO glass was sequentially cleaned with detergent water, deionized water, acetone, and isopropanol for 30 min in an

Key Laboratory of Advanced Light Conversion Materials and Biophotonics, Department of Chemistry, Renmin University of China, Beijing 100872, China. E-mail: cmu@ruc.edu.cn; xc.ai@ruc.edu.cn

† Electronic supplementary information (ESI) available. See <https://doi.org/10.1039/d2ra01913b>



ultrasonic system. Plasma treatment was performed for 3 min to enhance the surface wettability before spin coating the ETL solution. The pristine SnO_2 precursor solution was prepared from the SnO_2 colloidal solution by diluting 5 times with deionized water. The sample ETL solution was prepared by adding 4, 12 and 20 mg $\text{NiCl}_2 \cdot 6\text{H}_2\text{O}$ into the 4 mL mixed solvent, which comprise of 1 mL SnO_2 colloidal solution, 2 mL H_2O and 1 mL $\text{NH}_3 \cdot \text{H}_2\text{O}$. Ultimately the concentration of the $\text{NiCl}_2 \cdot 6\text{H}_2\text{O}$ was 1, 3 and 5 mg mL^{-1} . The sample ETL (SnO_2 - NiCl_2) solution was deposited on the FTO substrates at 4000 rpm for 30 s. The substrates were subsequently annealed in the air at 150 °C for 30 min to improve the electrical properties. After plasma treatment, the FTO substrates were transferred into a glove box. A perovskite precursor solution was prepared from the solution mixture of PbI_2 (1.67 M) and $\text{CH}_3\text{NH}_3\text{I}$ (1.67 M) in DMF/DMSO (7 : 3 by volume). The perovskite solution was spin coated on the substrate at 1000 rpm for 13 s and at 5000 rpm for 25 s. Three hundred microliters of CB was dropped on the substrates during the second step after 12–15 s, and the films were then annealed on the hot plate at 100 °C for 30 min. After the substrates cooled to room temperature, a HTL was formed by spin coating the spiro-OMeTAD precursor solution onto the surface of the perovskite film at 5000 rpm for 30 s, which was prepared by dissolving 58.4 mg of spiro-OMeTAD, 23 μL of tBp, 14 μL of LiTFSI (520 mg mL^{-1} acetonitrile), and 23 μL of FK209 (300 mg mL^{-1} acetonitrile) in 800 μL of chlorobenzene. Finally, an 80 nm gold electrode was deposited on the surface of the HTL under high-vacuum conditions.

Measurements and characterization

Scanning electron microscopy (SEM) images were obtained by a field emission scanning electron microscope (FE-SEM, Hitachi SU8010). X-ray diffraction (XRD) was conducted on a Shimadzu XRD7000 diffractometer using $\text{Cu K}\alpha$ radiation in the 2θ range from 10° to 60° at a scan rate of 2° min^{-1} . X-ray photoelectron spectroscopy (XPS) was performed using a Thermo KAlpha + instrument with an Al $\text{K}\alpha$ (1486.8 eV) X-ray source. UV-vis absorption spectra were recorded on an Agilent Cary 60 spectrometer. Steady-state photoluminescence (PL) and time-resolved PL (TRPL) spectroscopies were performed by an Edinburgh FLS 980 spectrometer. The current density–voltage (J - V) curves were measured by a Keithley 2400 source meter under simulated standardized sunlight (AM 1.5 G, 100 mW cm^{-2}) in ambient air. The devices were covered by a metal aperture mask to determine the 0.1 cm^2 active area. The incident photon-to-current efficiency (IPCE) was characterized by the photoelectric conversion test system (Enlitech QE-R). Electrochemical impedance spectroscopy (EIS) was performed using ZAHNER PP211 with a frequency range from 0.1 to 10⁶ Hz. The space charge limited current (SCLC) of the devices with FTO/ SnO_2 /perovskite/spiro/Au was measured on a Keithley 4200 from 0 to 2 V in the dark. In Transient photovoltage (TPV) measurements, the devices were illuminated by a light-emitting diode (LED, 520 ± 5 nm) to generate a different bias photovoltage (V_{ph}). A weak laser pulse (532 nm, 7 ns) was applied to generate a small perturbation. A series of desired V_{ph} values were

collected by adjusting the intensity of the LED. The results were recorded using a digital oscilloscope (Lecroy HDO4054A, coupling impedance: 1 M Ω). Transient photocurrent (TPC) results were recorded using the digital oscilloscope (input impedance of 50 Ω) after the TPV measurements.

Results and discussion

As shown in Fig. S1†, the introduction of $\text{NiCl}_2 \cdot 6\text{H}_2\text{O}$ did not change the crystal structure of SnO_2 . The higher transmittance of SnO_2 - NiCl_2 film in the visible region indicates that $\text{NiCl}_2 \cdot 6\text{H}_2\text{O}$ could reduce the light loss when light passing through the substrate. FTO/ SnO_2 films became smoother when the FTO substrate covered with a thin SnO_2 film. The smoother surface should be beneficial to the light transmission. SnO_2 films can improve the optical transmission properties of FTO substrates.^{33,34} Compared with FTO/ SnO_2 , FTO/ SnO_2 - NiCl_2 films were denser, and Ni^{2+} had the effect of antireflection, which promoted the increase of transmittance of FTO/ SnO_2 - NiCl_2 films in the visible region.^{35,36} Fig. 1a and b show the SEM images of the SnO_2 films without and with NiCl_2 , respectively. The introduction of $\text{NiCl}_2 \cdot 6\text{H}_2\text{O}$ improved surface compactness of the ETL, which can promote the formation of perovskite grains and performance of the device.³⁷

To confirm the successful introduction of nickel and chloride ions into the ETL, XPS was performed on different substrates. Fig. 1c shows the full XPS spectra of the corresponding ETLs. Fig. S4† shows energy dispersive spectroscopy (EDS) characterization of SnO_2 - NiCl_2 films. The results show

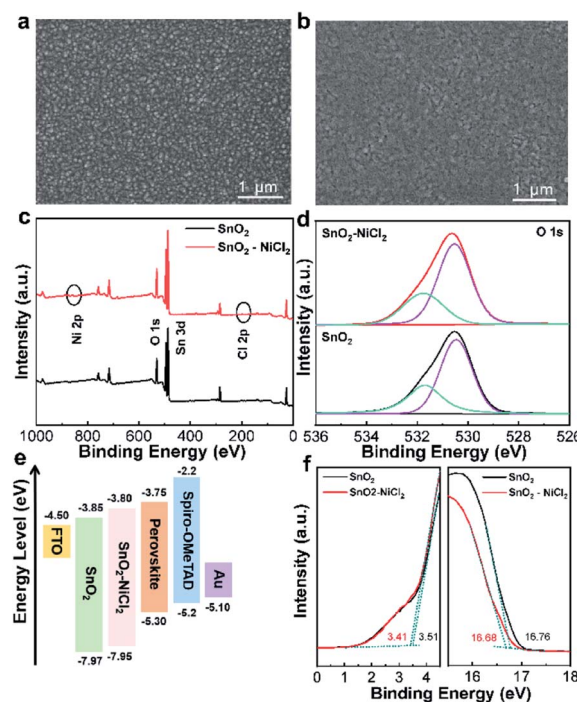


Fig. 1 ETLs using (a) pristine SnO_2 and (b) SnO_2 - NiCl_2 . (c) The XPS spectrum of SnO_2 and SnO_2 - NiCl_2 on FTO substrates. (d) XPS of O 1s. (e) Energy level diagram of PSCs. (f) UPS spectra of SnO_2 and SnO_2 - NiCl_2 films.

that the Ni, Cl, Sn, and O elements are uniformly distributed on the surface of the film. The enlarged XPS spectra are shown in Fig. S2 and S3†. The XPS spectra of $\text{SnO}_2\text{-NiCl}_2$ show characteristic peaks of Ni (855 eV) and Cl (198 eV) compared with unmodified SnO_2 . SnO_2 was deposited on FTO substrate, and it was annealed in the air at 150 °C for 30 min. In the annealing process, $[\text{Ni}(\text{NH}_3)_6]^{2+}$ by reaction with Ni^{2+} and $\text{NH}_3 \cdot \text{H}_2\text{O}$ would almost lose the NH_3 and H_2O when heated above 140 °C. The presence of Ni 2p_{3/2} at 855.6 eV, based on the binding energy position of XPS Ni 2p, indicates the transformation of Ni^{2+} into $\text{Ni}(\text{OH})_2$. $\text{Ni}(\text{OH})_2$ cannot further lose water to form NiO during annealing at 150 °C. The photoelectron binding energy of the Sn 3d level of $\text{SnO}_2\text{-NiCl}_2$ is slightly higher than that of the unmodified SnO_2 , indicating an interaction between SnO_2 and NiCl_2 . According to previous reports, the Ni^{2+} may play a more important role than Cl^- in improving the device performance of PSCs.³⁹ We presumed that the Ni^{2+} from NiCl_2 can interact with the hydroxyl groups ($-\text{OH}$) on the surface of the SnO_2 film, which can lead to a trap state, causing nonradiative recombination.⁴⁰ As shown in Fig. 1d and Table S1,† the peak at 530.46 eV was O–Sn bonds (or O^{2-} state), and the higher binding energy at 531.70 eV corresponded to hydroxyl groups (or oxygen vacancies). After the introduction of $\text{NiCl}_2 \cdot 6\text{H}_2\text{O}$, the intensity of hydroxyl (or oxygen vacancies) decreased significantly, indicating that the oxygen vacancies were effectively passivated.⁴¹ The reduction of oxygen vacancy defects will improve V_{OC} . Therefore, the successful introduction of $\text{NiCl}_2 \cdot 6\text{H}_2\text{O}$ will considerably improve the ETL.

Further characterizations were conducted to better understand the ETL/perovskite interface. Ultraviolet photoelectron spectroscopy (UPS) was performed to investigate the band structure of SnO_2 and $\text{SnO}_2\text{-NiCl}_2$. We tested the optimal concentration 3 mg mL^{−1}. The possible energy band alignment of planar PSCs was depicted in Fig. 1e. Combining with the high binding energy cutoff (E_{cutoff}) on the right side of Fig. 1f and the Fermi edge ($E_{\text{F,edge}}$) region on the left side of Fig. 1f, the value of E_{VB} could be calculated for SnO_2 and $\text{SnO}_2\text{-NiCl}_2$ at about −7.97 and −7.95 eV, respectively. We further confirmed the band gaps (E_{g}) of ETLs by the Tauc plots of UV-vis absorption spectra (Fig. S5†). The energy levels of the conduction band (E_{CB}) of SnO_2 and $\text{SnO}_2\text{-NiCl}_2$ were calculated to be −3.85 and −3.80 eV, respectively. According to the relative energy levels of the different PSC parts, the E_{CB} of the $\text{SnO}_2\text{-NiCl}_2$ ETL was higher than that of the SnO_2 ETL.⁴² The V_{OC} depends on the difference in energy between electron quasi Fermi level and hole quasi Fermi level.⁴³ More appropriate energy level would make the solar cell based on $\text{SnO}_2\text{-NiCl}_2$ show higher V_{OC} .

SEM characterization of the perovskite films prepared on SnO_2 and $\text{SnO}_2\text{-NiCl}_2$ substrates was performed, and the results are shown in Fig. 2a and b. The perovskite films prepared on the $\text{SnO}_2\text{-NiCl}_2$ substrates have larger grains and are generally compact, compared with the perovskite films prepared on SnO_2 . In addition, cracks obviously exist on the perovskite films prepared on SnO_2 , which lead to the recombination of electrons and holes.⁴⁴ The UV-vis absorption spectrum shown in Fig. 2c indicates that the bandgap of perovskite growing on the NiCl_2 -modified ETL has not changed. Fig. S6† presents the bandgap of

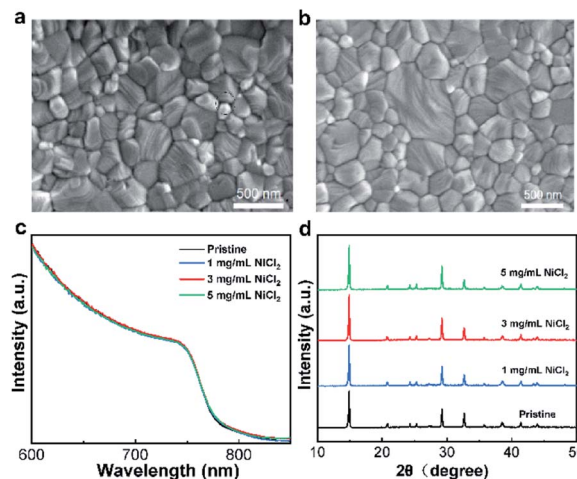


Fig. 2 Top view SEM images of perovskite films (a) with pristine SnO_2 and (b) $\text{SnO}_2\text{-NiCl}_2$. (c) The absorbance of perovskite films based on SnO_2 and $\text{SnO}_2\text{-NiCl}_2$. (d) The XRD pattern of perovskite films with different concentrations of $\text{SnO}_2\text{-NiCl}_2$.

perovskite grown on ETL with and without $\text{NiCl}_2 \cdot 6\text{H}_2\text{O}$, and the calculated bandgap value is 1.61 eV. XRD analyses were performed to characterize the crystal structure of perovskite, as shown in Fig. 2d. The results show that the characteristic diffraction peaks of $\text{CH}_3\text{NH}_3\text{PbI}_3$ appear near 14.1°, 24.5°, 28.5°, 31.6°, and 40.4°, which correspond to the crystal planes of (110), (202), (220), (310), and (224) of $\text{CH}_3\text{NH}_3\text{PbI}_3$, respectively.^{45,46} These results confirm that perovskite films with good crystallinity were prepared by introducing $\text{NiCl}_2 \cdot 6\text{H}_2\text{O}$.

To study the carrier transport in PSCs, steady-state fluorescence spectroscopy (PL) experiments were performed on the perovskite films on SnO_2 and $\text{SnO}_2\text{-NiCl}_2$ substrates.^{47,48} As shown in Fig. 3a, carrier quenching was slower for the samples on the $\text{SnO}_2\text{-NiCl}_2$ substrates, which is detrimental to increasing J_{SC} of the solar cell. However, the transmittance of the tin dioxide layer was increased after modification by $\text{NiCl}_2 \cdot 6\text{H}_2\text{O}$, the utilization rate of photons will be improved and J_{SC} will increase. Overall, the J_{SC} of the device based on $\text{SnO}_2\text{-NiCl}_2$ was a little better than that of the SnO_2 solar cell. The reason of the carrier quenching was slow for the samples on the $\text{SnO}_2\text{-NiCl}_2$ substrates was the passivation of chloride ions, which suppressed the nonradiative recombination of perovskite films for the enhancing intensity and the larger perovskite grain

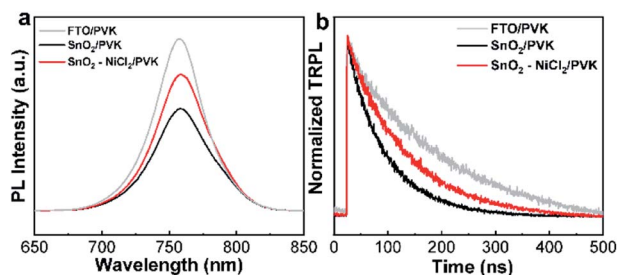


Fig. 3 (a) The PL and (b) TRPL spectra of MAPbI_3 without and with NiCl_2 .



size.⁴⁰ In Fig. 3b, the biexponential decay behavior is evident on the TRPL spectrum. We calculated the decay times (e.g., τ_1 and τ_2) of the perovskite film deposited on the SnO₂ and SnO₂-NiCl₂ substrates; the fitting parameters are summarized in Table S2.† PL decay process consists of a carrier recombination process in the bulk region, as characterized by the slow decay lifetime τ_2 , as well as a charge-transfer process at the interface, as characterized by the fast lifetime τ_1 . According to the results of the double exponential fitting in TRPL τ_1 increases, show that charge extraction at a slower pace and it will cause a decline in J_{SC} . τ_2 increases, and combining with SCLC and EIS data, shows that tin oxide layer of oxygen vacancy defects passivation, V_{OC} increases. The average decay time of the SnO₂/perovskite film is 70.62 ns, and the perovskite film deposited on SnO₂-NiCl₂ exhibited slower fluorescence quenching with an average decay time of 107.1 ns. The results were consistent with PL conclusions.

To justify the photoelectric performance of the PSCs caused by the introduction of NiCl₂·6H₂O, SCLC analyses were performed on the SnO₂ and SnO₂-NiCl₂ ETLs. The results are shown in Fig. 4a and b, including the calculated density of defect states. The defect density between the interface of ETL and the perovskite layer can partially reflect the contact and matching degree between interfaces. In the SCLC analyses, there is a clear linear relationship between the current and low bias voltage, which becomes non-linear as the voltage increases. The bias voltage of different substrates can be obtained from the SCLC curve, and the defect density can be subsequently calculated according to the formula of $N_t = 2\epsilon\epsilon_0 V_{TFL}/eL^2$, where V_{TFL} is the trap-filled-limit voltage marked in Fig. 4a and b, e is the elementary charge, L is the thickness of the perovskite film, ϵ is the dielectric constant, and ϵ_0 is the vacuum permittivity. According to the single calculation of the SCLC results, the bias voltage of the SnO₂-NiCl₂ substrate decreased from 0.930 V to 0.810 V, indicating a tendency of the defect state between the ETL and the perovskite layer to decrease after NiCl₂ modification. After further calculation obtained defect concrete values, the trap

densities of perovskite film deposited on pristine SnO₂ and SnO₂-NiCl₂ ETL are $1.45 \times 10^{16} \text{ cm}^{-3}$ and $1.26 \times 10^{16} \text{ cm}^{-3}$.

We further elucidated the effect of NiCl₂ on the defects of the SnO₂ film by measuring the recombination dynamics, transient photovoltage (TPV), and transient photocurrent (TPC) decay. As shown in Fig. 4c, the carrier recombination lifetime of the device with SnO₂-NiCl₂ increased from 22.65 to 35.33 μs , confirming the suppressed charge recombination at the ETL and perovskite interface. For the transport time constants (τ_t) measured from TPC (Fig. 4d), PSCs based on SnO₂-NiCl₂ exhibited 0.67 μs compared to that of the pristine SnO₂-based PSCs (0.93 μs).^{49,50}

To investigate the effect of SnO₂-NiCl₂ ETL on device performance, we fabricated PSCs with the FTO/ETL/MAPbI₃/Spiro-OMeTAD/Au (Fig. 5a) structure and investigated the doping concentration of NiCl₂·6H₂O in SnO₂. The devices were prepared with the concentration of SnO₂ precursor solution (1, 3 and 5 mg mL⁻¹) and annealing at 150 °C for 30 min. Electrochemical impedance spectroscopy (EIS) analyses were performed on devices composed of SnO₂ and SnO₂-NiCl₂ substrates,^{51–53} and the results are shown in Fig. 5b. In the dark state condition, within the frequency range of 0.1 to 10⁶ Hz, the transmission electricity of the SnO₂-based cell was measured. By fitting the measured results, the contact resistance (R_s) and recombination resistance (R_{rec}) values of the PSCs employing pristine SnO₂ and SnO₂-NiCl₂ are summarized in Table S3.† The small semicircle at high frequency corresponds to the charge transfer process between perovskite and selective

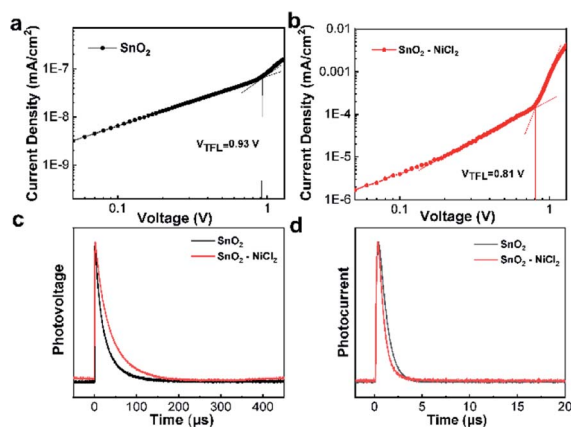


Fig. 4 SCLC measurements of devices (a) with pristine SnO₂ and (b) SnO₂-NiCl₂. (c) Transient photovoltage decay curves of PSCs based on pristine SnO₂ and SnO₂-NiCl₂. (d) Transient photocurrent decay curves of PSCs based on pristine SnO₂ and SnO₂-NiCl₂.

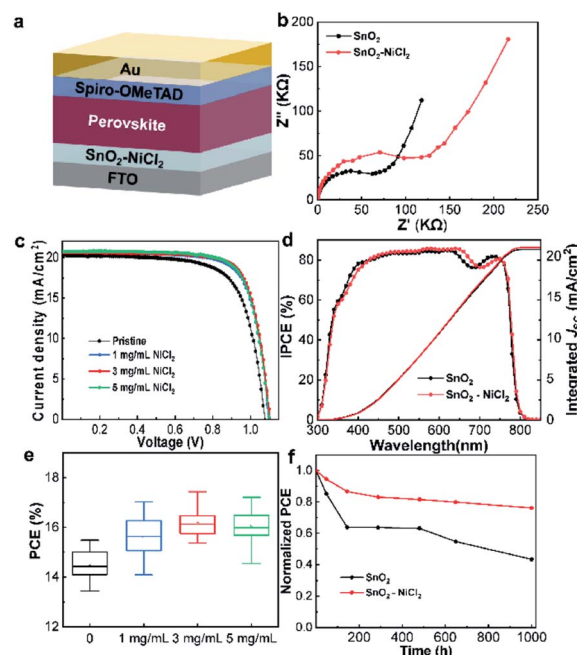


Fig. 5 (a) Device architecture. (b) Nyquist plots. (c) J - V characteristics of the best devices with different nickel chloride concentrations. (d) External quantum efficiency of PSCs based on pristine SnO₂ and SnO₂-NiCl₂. (e) Device performance of PSCs based on SnO₂ with different concentrations of NiCl₂. (f) Stability measurements of PSCs based on pristine SnO₂ and SnO₂-NiCl₂ under a N₂ atmosphere.



Table 1 Photovoltaic parameters of cells based on SnO₂ and SnO₂-NiCl₂ films with different additive concentrations

Samples	V _{OC} (V)	J _{SC} (mA cm ⁻²)	FF (%)	PCE (%)
Pristine	1.078	20.21	0.711	15.49
1 mg mL ⁻¹ NiCl ₂	1.098	20.70	0.749	17.02
3 mg mL ⁻¹ NiCl ₂	1.104	20.59	0.764	17.36
5 mg mL ⁻¹ NiCl ₂	1.100	20.70	0.756	17.21

contacts while the large semicircle at low frequency demonstrates the recombination of charge carriers in the perovskite layer.⁵⁴ Through EIS test, the results show that the transmission resistance R_s and the composite resistance R_{rec} increased, indicating that the charge transmission speed slowed down and the defect was effectively passivated. However, because the transmittance of the tin dioxide layer increased after modification, the utilization rate of photons will be improved and J_{SC} will increase. The results were consistent with the fluorescence and efficiency data.⁵² Simultaneously, it was beneficial to improve V_{OC} of the device.⁵³

The corresponding J - V curves are shown in Fig. 5c and S7.† The results show that the device performance slightly improved with SnO₂-NiCl₂ concentration of 1 mg mL⁻¹. The highest open-circuit voltage (V_{OC}), FF, and PCE values of the PSCs were obtained with SnO₂-NiCl₂ concentration of 3 mg mL⁻¹. When the doping NiCl₂·6H₂O amount further increased, the photoelectric performance of the device decreased, and thus the optimum concentration of SnO₂-NiCl₂ was 3 mg mL⁻¹.

Subsequently, the IPCE of the optimum NiCl₂·6H₂O and control devices were tested. As shown in Fig. 5d, the light absorption capacity of the NiCl₂-modified devices in the range of 400–700 nm was stronger than that of the SnO₂-based devices, corresponding to a higher current. The results show that the introduction of NiCl₂·6H₂O could effectively improve the ability of the ETL to light transmission. The integrated J_{SC} value measured by IPCE was consistent with the J_{SC} obtained by the J - V curves.

The statistical distribution of PCE for PSCs based on doped ETLs of different NiCl₂·6H₂O concentrations are shown in Fig. 5e and S8.† The PCE of the SnO₂-based devices ranged between 14%–16% and the PCE of the SnO₂-NiCl₂-based devices was in the range of 16%–18%. As shown in Table 1, the modified device exhibits a PCE of 17.36% with a J_{SC} of 20.59 mA cm⁻², V_{OC} of 1.104 V, and FF of 76.4%. Devices based on the SnO₂-NiCl₂ ETL also exhibit greater stability than the reference devices (Fig. 5f). The SnO₂-NiCl₂-based PSCs can retain 76% of their initial efficiency after being stored for 1000 h at the room temperature (RT) of 25 °C for 1000 h. In contrast, the reference devices only retained 43% of their initial efficiency. This may be due to the larger grain size with fewer grain boundaries which offers additional protection against oxygen and moisture.

Conclusions

In this study, we provide a simple and effective method to modify SnO₂ ETL with NiCl₂·6H₂O, which reduced the oxygen vacancies of SnO₂ and improved the energy level alignment.

This modification ultimately dramatically passivated defects, which effectively improved the V_{OC} and PCE. Notably, the stability of the SnO₂-NiCl₂-based PSCs increased, and was able to maintain 76% of the original PCE after 1000 h of storage, compared to 43% for the device without NiCl₂·6H₂O.

Conflicts of interest

There are no conflicts to declare.

Acknowledgements

The authors acknowledge financial support from the National Key R&D Program of China (Grant no. 2018YFA0208701), National Natural Science Foundation of China (Grant no. 21773308), the Research Funds of Renmin University of China (Grant no. 201903020).

Notes and references

- Q. Chen, N. De Marco, Y. Yang, T.-B. Song, C.-C. Chen, H. Zhao, Z. Hong, H. Zhou and Y. Yang, *Nano Today*, 2015, **10**, 355–396.
- M. A. Green, A. Ho-Baillie and H. J. Snaith, *Nat. Photonics*, 2014, **8**, 506–514.
- G. Xing, N. Mathews, S. Sun, S. S. Lim, Y. M. Lam, M. Gratzel, S. Mhaisalkar and T. C. Sum, *Science*, 2013, **342**, 344–347.
- H. Min, M. Kim, S. U. Lee, H. Kim, G. Kim, K. Choi, J. H. Lee and S. I. Seok, *Science*, 2019, **366**, 749–753.
- M. Abdi-Jalebi, Z. Andaji-Garmaroudi, S. Cacovich, C. Stavrakas, B. Philippe, J. M. Richter, M. Alsari, E. P. Booker, E. M. Hutter, A. J. Pearson, S. Lilliu, T. J. Savenije, H. Rensmo, G. Divitini, C. Ducati, R. H. Friend and S. D. Stranks, *Nature*, 2018, **555**, 497–501.
- W. S. Yang, B. W. Park, E. H. Jung, N. J. Jeon, Y. C. Kim, D. U. Lee, S. S. Shin, J. Seo, E. K. Kim, J. H. Noh and S. I. Seok, *Science*, 2017, **356**, 1376–1379.
- W. S. Yang, J. H. Noh, N. J. Jeon, Y. C. Kim, S. Ryu, J. Seo and S. I. Seok, *Science*, 2015, **348**, 1234–1237.
- K. Xiao, R. Lin, Q. Han, Y. Hou, Z. Qin, H. T. Nguyen, J. Wen, M. Wei, V. Yeddu, M. I. Saidaminov, Y. Gao, X. Luo, Y. Wang, H. Gao, C. Zhang, J. Xu, J. Zhu, E. H. Sargent and H. Tan, *Nat. Energy*, 2020, **5**, 870–880.
- M. Jeong, I. W. Choi, E. M. Go, Y. Cho, M. Kim, B. Lee, S. Jeong, Y. Jo, H. W. Choi, J. Lee, J. H. Bae, S. K. Kwak, D. S. Kim and C. Yang, *Science*, 2020, **369**, 1615–1620.
- R. Lin, K. Xiao, Z. Qin, Q. Han, C. Zhang, M. Wei, M. I. Saidaminov, Y. Gao, J. Xu, M. Xiao, A. Li, J. Zhu, E. H. Sargent and H. Tan, *Nat. Energy*, 2019, **4**, 864–873.
- M. Saliba, T. Matsui, J. Y. Seo, K. Domanski, J. P. Correa-Baena, M. K. Nazeeruddin, S. M. Zakeeruddin, W. Tress, A. Abate, A. Hagfeldt and M. Gratzel, *Energy Environ. Sci.*, 2016, **9**, 1989–1997.
- H. Min, D. Y. Lee, J. Kim, G. Kim, K. S. Lee, J. Kim, M. J. Paik, Y. K. Kim, K. S. Kim, M. G. Kim, T. J. Shin and S. I. Seok, *Nature*, 2021, **598**, 444–450.



- 13 W. Xu, X. Yao, H. Wu, T. Zhu and X. Gong, *Emergent Mater.*, 2020, **3**, 727–750.
- 14 X. Zhao, L. Tao, H. Li, W. Huang, P. Sun, J. Liu, S. Liu, Q. Sun, Z. Cui, L. Sun, Y. Shen, Y. Yang and M. Wang, *Nano Lett.*, 2018, **18**, 2442–2449.
- 15 Y. Wu, X. Yang, W. Chen, Y. Yue, M. Cai, F. Xie, E. Bi, A. Islam and L. Han, *Nat. Energy*, 2016, **1**, 16148.
- 16 Z. Zhu, C. C. Chueh, F. Lin and A. K. Jen, *Adv. Sci. (Weinh.)*, 2016, **3**, 1600027.
- 17 G. Grancini, C. Roldan-Carmona, I. Zimmermann, E. Mosconi, X. Lee, D. Martineau, S. Narbey, F. Oswald, F. De Angelis, M. Graetzel and M. K. Nazeeruddin, *Nat. Commun.*, 2017, **8**, 15684.
- 18 P. W. Liang, C. Y. Liao, C. C. Chueh, F. Zuo, S. T. Williams, X. K. Xin, J. Lin and A. K. Jen, *Adv. Mater.*, 2014, **26**, 3748–3754.
- 19 C. Zuo and L. Ding, *Nanoscale*, 2014, **6**, 9935–9938.
- 20 W. Ke, C. Xiao, C. Wang, B. Saparov, H. S. Duan, D. Zhao, Z. Xiao, P. Schulz, S. P. Harvey, W. Liao, W. Meng, Y. Yu, A. J. Cimaroli, C. S. Jiang, K. Zhu, M. Al-Jassim, G. Fang, D. B. Mitzi and Y. Yan, *Adv. Mater.*, 2016, **28**, 5214–5221.
- 21 Y. Wu, F. Xie, H. Chen, X. Yang, H. Su, M. Cai, Z. Zhou, T. Noda and L. Han, *Adv. Mater.*, 2017, **29**, 1701073.
- 22 F. Wang, W. Geng, Y. Zhou, H. H. Fang, C. J. Tong, M. A. Loi, L. M. Liu and N. Zhao, *Adv. Mater.*, 2016, **28**, 9986–9992.
- 23 H. S. Kim, C. R. Lee, J. H. Im, K. B. Lee, T. Moehl, A. Marchioro, S. J. Moon, R. Humphry-Baker, J. H. Yum, J. E. Moser, M. Gratzel and N. G. Park, *Sci. Rep.*, 2012, **2**, 591.
- 24 M. M. Lee, J. Teuscher, T. Miyasaka, T. N. Murakami and H. J. Snaith, *Science*, 2012, **338**, 643–647.
- 25 R. Meng, X. Feng, Y. Yang, X. Lv, J. Cao and Y. Tang, *ACS Appl. Mater. Interfaces*, 2019, **11**, 13273–13278.
- 26 A. K. Kadhim, M. R. Mohammad and A. I. Abd Ali, *Chem. Phys. Lett.*, 2022, **786**, 139189.
- 27 G. Liu, Z. Liu, L. Wang, K. Zhang and X. Xie, *Chem. Phys. Lett.*, 2021, **771**, 138496.
- 28 F. Wang, M. Yang, Y. Zhang, J. Du, S. Yang, L. Yang, L. Fan, Y. Sui, Y. Sun and J. Yang, *Nano Res.*, 2021, **14**, 2783–2789.
- 29 Q. Zhuang, H. Wang, C. Zhang, C. Gong, H. Li, J. Chen and Z. Zang, *Nano Res.*, 2022, DOI: [10.1007/s12274-022-4135-7](https://doi.org/10.1007/s12274-022-4135-7).
- 30 S. Wendt, P. T. Sprunger, E. Lira, G. K. Madsen, Z. Li, J. O. Hansen, J. Matthiesen, A. Blekinge-Rasmussen, E. Laegsgaard, B. Hammer and F. Besenbacher, *Science*, 2008, **320**, 1755–1759.
- 31 D. Yang, R. Yang, K. Wang, C. Wu, X. Zhu, J. Feng, X. Ren, G. Fang, S. Priya and S. F. Liu, *Nat. Commun.*, 2018, **9**, 3239.
- 32 T. Yang, X. Qin, H.-h. Wang, Q. Jia, R. Yu, B. Wang, J. Wang, K. Ibrahim, X. Jiang and Q. He, *Thin Solid Films*, 2010, **518**, 5542–5545.
- 33 W. Ke, G. Fang, Q. Liu, L. Xiong, P. Qin, H. Tao, J. Wang, H. Lei, B. Li, J. Wan, G. Yang and Y. Yan, *J. Am. Chem. Soc.*, 2015, **137**, 6730–6733.
- 34 Y. Luan, X. Yi, P. Mao, Y. Wei, J. Zhuang, N. Chen, T. Lin, C. Li and J. Wang, *iScience*, 2019, **16**, 433–441.
- 35 Y. Chen, X. Zuo, Y. He, F. Qian, S. Zuo, Y. Zhang, L. Liang, Z. Chen, K. Zhao, Z. Liu, J. Gou and S. F. Liu, *Adv. Sci. (Weinh.)*, 2021, **8**, 2001466.
- 36 Z. Qian, L. Chen, J. Wang, L. Wang, Y. Xia, X. Ran, P. Li, Q. Zhong, L. Song, P. Müller-Buschbaum, Y. Chen and H. Zhang, *Adv. Mater. Interfaces*, 2021, **8**, 2100128.
- 37 B. Y. Gao, Q. Cao, X. Y. Pu, J. B. Yang, J. Han, S. J. Wang, T. T. Li, Z. W. He and X. H. Li, *Appl. Surf. Sci.*, 2021, **546**, 148711.
- 38 L. Zhu, Q. Lu, C. Li, Y. Wang and Z. Deng, *Chin. Chem. Lett.*, 2021, **32**, 2259–2262.
- 39 D. Wang, C. Wu, X. Qi, W. Luo, Y. Zhang, Z. Zhang, X. Guo, B. Qu, L. Xiao and Z. Chen, *ACS Appl. Energy Mater.*, 2019, **2**, 5883–5888.
- 40 P. Wang, B. Chen, R. Li, S. Wang, N. Ren, Y. Li, S. Mazumdar, B. Shi, Y. Zhao and X. Zhang, *ACS Energy Lett.*, 2021, **6**, 2121–2128.
- 41 D. Wang, T. He, S. Li, Y. Jiang and M. Yuan, *ACS Appl. Energy Mater.*, 2021, DOI: [10.1021/acsaem.1c02666](https://doi.org/10.1021/acsaem.1c02666).
- 42 J. Yan, Z. Lin, Q. Cai, X. Wen and C. Mu, *ACS Appl. Energy Mater.*, 2020, **3**, 3504–3511.
- 43 P. Caprioglio, M. Stollerfoht, C. M. Wolff, T. Unold, B. Rech, S. Albrecht and D. Neher, *Adv. Energy Mater.*, 2019, **9**, 1901631.
- 44 X. Liu, Y. Zhang, L. Shi, Z. Liu, J. Huang, J. S. Yun, Y. Zeng, A. Pu, K. Sun, Z. Hameiri, J. A. Stride, J. Seidel, M. A. Green and X. Hao, *Adv. Energy Mater.*, 2018, **8**, 1800138.
- 45 S. Sidhik, A. Cerdan Pasaran, D. Esparza, T. Lopez Luke, R. Carriles and E. De la Rosa, *ACS Appl. Mater. Interfaces*, 2018, **10**, 3571–3580.
- 46 J. Cao, X. Lv, P. Zhang, T. T. Chuong, B. Wu, X. Feng, C. Shan, J. Liu and Y. Tang, *Adv. Mater.*, 2018, **30**, e1800568.
- 47 M. Kim, G.-H. Kim, T. K. Lee, I. W. Choi, H. W. Choi, Y. Jo, Y. J. Yoon, J. W. Kim, J. Lee, D. Huh, H. Lee, S. K. Kwak, J. Y. Kim and D. S. Kim, *Joule*, 2019, **3**, 2179–2192.
- 48 M. Sun, J. Shu, C. Zhao, J. Wu, H. Guo, Y. Guo, X. Yin, Y. Lin, Z. Tan, M. He and L. Wang, *ACS Appl. Mater. Interfaces*, 2022, **14**, 13352–13360.
- 49 J. W. Jung, S. T. Williams and A. K. Y. Jen, *RSC Adv.*, 2014, **4**, 62971–62977.
- 50 Y. Liu, Q. Chen, H.-S. Duan, H. Zhou, Y. Yang, H. Chen, S. Luo, T.-B. Song, L. Dou, Z. Hong and Y. Yang, *J. Mater. Chem. A*, 2015, **3**, 11940–11947.
- 51 K. Liu, S. Chen, J. Wu, H. Zhang, M. Qin, X. Lu, Y. Tu, Q. Meng and X. Zhan, *Energy Environ. Sci.*, 2018, **11**, 3463–3471.
- 52 H. S. Kim, J. W. Lee, N. Yantara, P. P. Boix, S. A. Kulkarni, S. Mhaisalkar, M. Gratzel and N. G. Park, *Nano Lett.*, 2013, **13**, 2412–2417.
- 53 T. Zhu, Y. Yang, S. Zhou, X. Yao, L. Liu, W. Hu and X. Gong, *Chin. Chem. Lett.*, 2020, **31**, 2249–2253.
- 54 N. D. Pham, V. T. Tiong, P. Chen, L. Wang, G. J. Wilson, J. Bell and H. Wang, *J. Mater. Chem. A*, 2017, **5**, 5195–5203.

